ISOPHOT-S spectral atlas of Young Stellar Objects

P. Ábrahám, A. Moór and M. Kun

Konkoly Observatory of the Hungarian Academy of Sciences, P.O.Box 67, H-1525 Budapest, Hungary

1. Motivation

ISOPHOT-S was a sub-instrument of ISOPHOT on-board the *Infrared Space Observatory* (ISO). It produced low-resolution mid-infrared spectra of 128 points covering the 2.5–4.9 and 5.8–11.6μm wavelength ranges with a spectral resolution of $R \sim$100, during the active period of ISO (1995–98). The aperture was $24'' \times 24''$. The typical absolute photometric accuracy was 8-10% at high flux level and 40-50 mJy at low flux level (slightly depending on pixel and exposure time), thus ISOPHOT-S was more sensitive than the ISO-SWS instrument. For a detailed description of ISOPHOT-S see Acosta-Pulido & Ábrahám (2003).

The ISOPHOT-S observations provide possibilities of studying the PAH-bands at 6.3, 7.7, 8.6 and 11.3 μm, of defining the short wavelength continuum of the 10μm silicate feature, and – since the spectra are absolutely calibrated – of supplementing spectral energy distributions. An ISOPHOT-S spectral atlas could also serve as the preparatory database for both ground (e.g. VLT/MIDI) and space based (Spitzer, Herschel) observations.

Though the ISO Legacy Archive contains reliable results for most ISOPHOT-S observations, several instrumental artifacts were discovered after the closure of the Archive. We have developed an IDL-based processing package aiming at correcting these artifacts. This new scheme was applied on a set of young stellar object observations, leading to the construction of the present Highly Processed Data Product in the form of a spectral atlas.

2. Source selection and data reduction

2.1. Extraction of YSO observations from the ISO Data Archive

We made a query of the ISO Data Archive for ISOPHOT-S observations (AOT PHT40) and selected observations of young stellar objects via consulting with SIMBAD and with the literature. The query resulted in 162 measurements of 135 YSOs (162/135). In the present spectral atlas we included 82 observations of 64 YSOs, which could be further categorized as follows: I. Embedded low- and intermediate-mass objects (5/5); II. Low-mass young stars

(28/22); III. Intermediate mass stars (41/33); IV. Eruptive young stellar objects (EXors, FUors) (8/4).

Most observations consist of separate ON/OFF measurements (72 measurements), but chopping between the source and background positions (9), as well as small scans/maps (1) were also utilized. The data from the ISO Data Archive were retrieved as Edited Raw Data (ERD) files, and were then processed in batch mode with the Phot Interactive Analysis (PIA) V10.0 software. A review of the PHT-S calibration strategies was presented in Acosta-Pulido & Ábrahám (2003).

2.2. Interactive post-processing of the observations

In the following we describe our IDL-based processing package. Possible correction algorithms were tested and optimized on a set of 43 normal star measurements, and the same data set was used to estimate typical measurement uncertainties via comparison with photospheric models. The processing scheme consists of the following steps:

Deglitching. As a preparation, we checked whether PIA had successfully removed all cosmic glitches from the data. The PIA built-in deglitching algorithms are quite efficient, nevertheless we often experienced that in observations of very faint sources glitches were still present, producing artificial spikes in the spectra. The reason is that at low signal level the recovery from a cosmic hit takes a relatively long time, and the disturbance following the hit may have a characteristic timescale comparable to the full measurement time (for an example see Fig. 1). In such a situation the statistical algorithms of PIA – which assume that the majority of the signals are not affected by glitches – do not work properly. In order to identify the remaining glitches the signal evolution of each pixel was visually inspected at the SRD processing level, and – when necessary – the affected data points were manually discarded using PIA.

Detector temperature and orbital phase. Before entering the processing, we checked two parameters which are related to the data quality. It was already demonstrated during the ISO mission that when the detector temperature was outside the nominal 2.8–3.1 K range, the transient behaviour might have differed from the usual one, leading to systematic photometric errors. Also, observations obtained either at the very beginning or the very end of the orbit might have suffered from reduced accuracy due to a higher dark current and to a higher cosmic glitch rate, respectively. For the time being none of the two effects can be

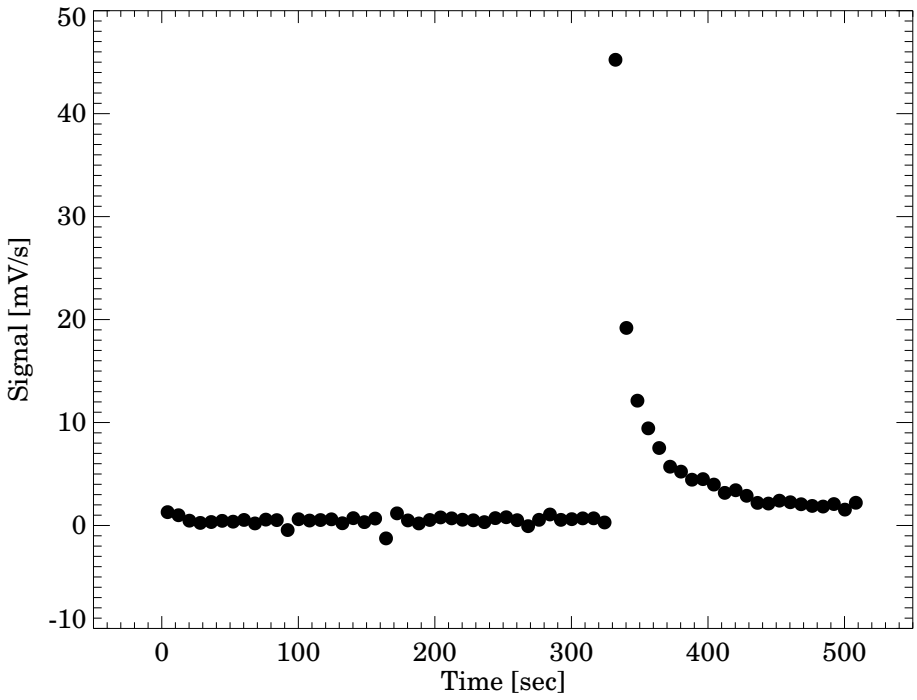

Fig. 1.— *Example for a cosmic glitch which was only partly corrected by the standard PIA de-glitching algorithm, producing a spike in the spectrum (HD 97300, ISO_id=62501316, Pix.=60). In our interactive processing all data point after t=330 sec are manually discarded.*

quantitatively characterized or corrected, but they seem usually be less important than the corrections described in the following paragraps.

Signal memory from preceeding observation. We found the appearance of artificial spectral features in some spectra due to memory effects from a preceeding bright observation. In order to identify affected spectra we studied the short (32 sec) dark measurements performed before each PHT-S observation. Reducing the complete sample of these measurements from the mission we determined their average signal levels and typical measurement uncertainties per pixel. If the measured short dark signal of a particular observation exceeded the average level by more than 1σ for a a continuous section of the spectrum (i.e. for a group of neighbouring pixels) than the observation was flagged for memory effect. Figure 2 presents an example. From tests on cases where external information on the spectral shape (theoretical models; TIMMI2 observations) was available, we concluded that subtracting the excess of the short dark signal from the astronomical observation per pixel can efficiently

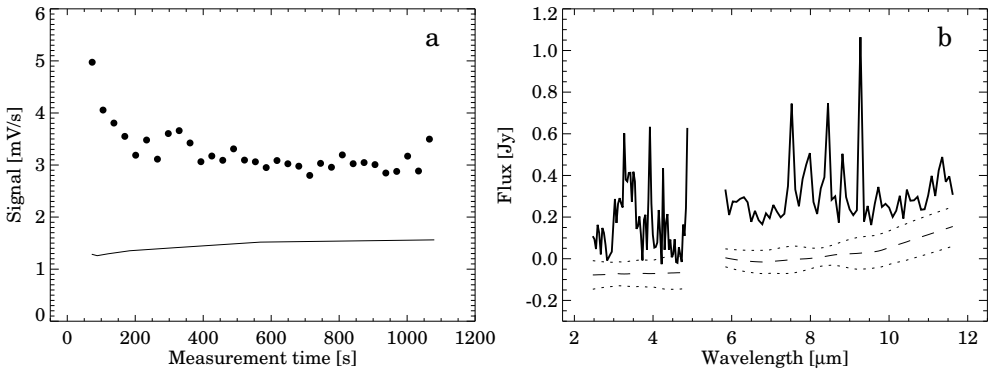

Fig. 2.— *Example for memory effect in ISO_id=62501703. (a) the measured signal of Pix. 93 (λ=8.45 μm) decreases rather than increases with time, due to recent illumination of the pixel by a bright source. The measured signals lie above the expected transient curve (continuous line), leading to an overestimation of the derived flux. (b) the flux excess is also visible when the measured short dark signal is compared with the mission average value.*

correct for the memory effect.

Background subtraction. There are a number of spectrophotometric observations where no corresponding sky background measurement has been performed. In the wavelength range of PHT-S the dominant background component is the zodiacal light (apart from localised regions like HII regions, reflection nebulae, or the galactic plane). In the 5.8–11.7 μm regime the zodiacal flux was clearly measurable for PHT-S (see Leinert et al., 2002), and its contribution is not negligible in the case of fainter stars (see Fig. 3). We created a model which was able to predict the spectrum of the zodiacal background towards a given direction and on a given date. The algorithm used 4.8 and 12 μm photometric points from COBE/DIRBE photometry as input; connected them with a Planck-curve; and finally scaled with a wavelength- and observing time-dependent factor optimized for the 29 high quality PHT-S spectra of the Zodiacal Light presented in Leinert et al. (2002).

Special processing of spectral maps. There are a few sources which were measured in mapping mode (usually 1D scans). The target is usually situated on the central map position, and the neighbouring raster steps can be used to obtain a background spectrum interpolated for the source's position. The mapping mode had several advantages over the typical ON–OFF staring observations, because it provides a well-measured background, and the subtraction of the interpolated background cancels automatically any memory effect, thus the algorithm described above is not used here. It is a problem, however, that the successful

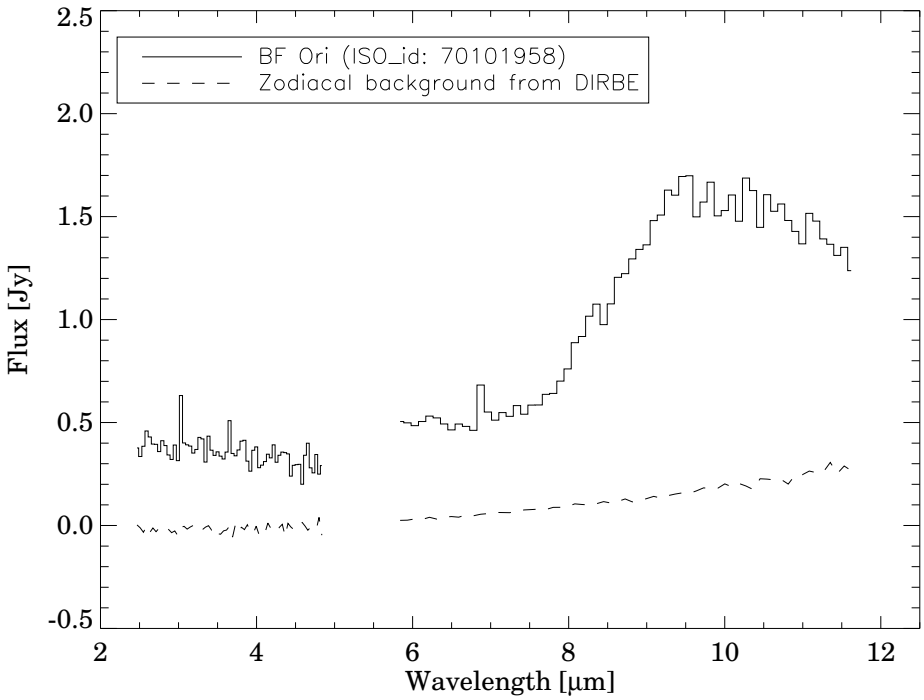

Fig. 3.— *Contribution of the zodiacal background to the measured flux of BF Ori. Since no dedicated background measurement was performed, the zodiacal spectrum was estimated from the DIRBE 4.9 and 12 μm data points extracted for the position and date of the BF Ori observation.*

Dynamic response calibration method (see Acosta-Pulido & Ábrahám 2003) was developed for staring observations, and in the standard processing scheme maps are calibrated by means of a static spectral response function. This method, however, cannot cope with the different transient timescales of the different detector pixels, and may produce obvious spectral artifacts. In order to find an alternative solution, we tested a simple algorithm which considers the time sequence of the map as a long staring observation, applies Dynamic response calibration on it, and creates a map from the calibrated flux values. The results looked convincing to us, because of the lack of any obvious spectral artifacts, and because of the good agreement with the ISOPHOT photometry. Raster observations presented in the atlas were processed using this algorithm.

Off-centre position of the source in the beam. The footprints of the PHT-S pixels were peaked rather than flat-top, therefore observing a compact source outside the optical axis of the pixel could change the measured signal. Since the calibration was set up for

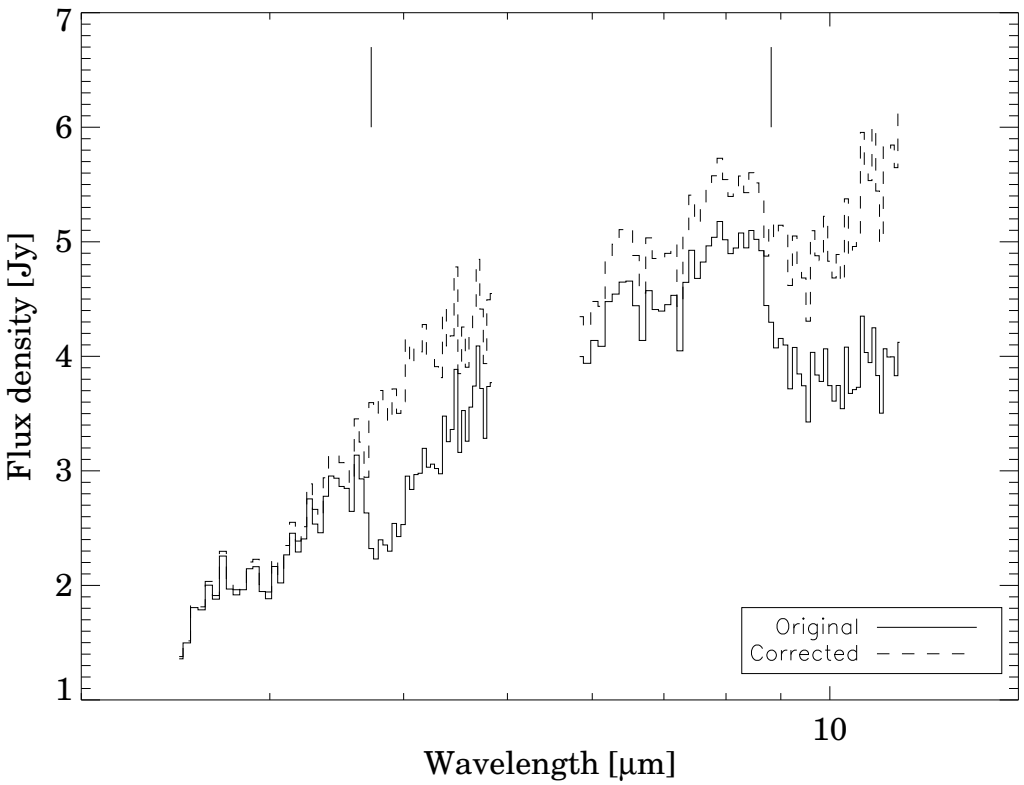

Fig. 4.— *Example for spectral artifacts introduced by off-centre location of a point source in the PHT-S beam. The object (Ced 112 IRS 4, ISO_id:62501217) was offset by* $+4.8''$ *and* $-0.6''$ *in satellite Y- and Z-direction, respectively. Vertical marks show the wavelengths where the most obvious artifacts, in the forms of discontinuities, appear.*

the pixel centre, off-centre observations have to be corrected in order to derive their correct flux values. In addition, because the footprint profiles varied with wavelength (there were especially large jumps at 3.7 and 8.8 μm) off-centre position lead to the appearance of spectral artifacts, too (an example is shown in Fig. 4). In order to correct for both the incorrect flux values and the spectral artifacts, we determined the offset of the source from the centre by comparing the accurate position of the object with ISO's coordinates. The 2-dimensional footprint map (we utilised the ones derived by Leinert et al. 2002) was then sampled at the offset position, and the measured flux was scaled with the ratio between footprint values at the centre and at the offset location. This procedure was repeated for each detector pixel independently. For accurate source positions we consulted the 2MASS catalog or SIMBAD; if no coordinates better than $1''$ were available then no correction was performed.

Empirical photometric correction. In order to check for any remaining systematic effects in the final photometry, we querried the Archive, collected all normal star observations,

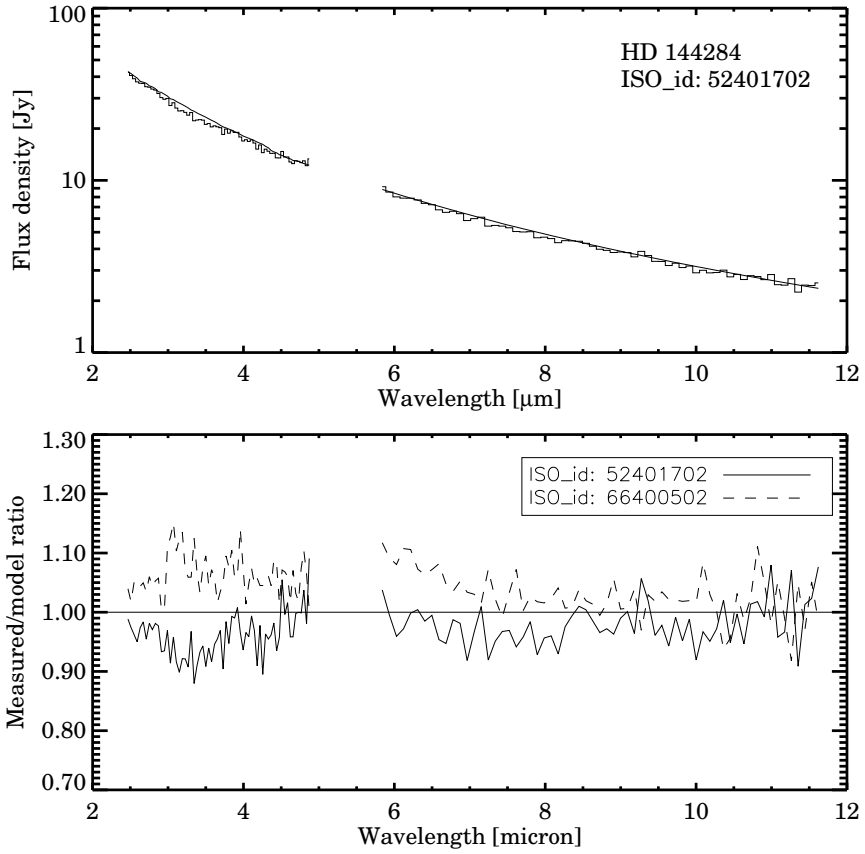

Fig. 5.— *Upper panel: Spectrum of the standard star HD 144284 (histogram) compared with model prediction (solid line). Lower panel: Ratio of measured flux values to model prediction for two independent observations of HD 144284.*

and reduced them in the way described above. Fig. 5 shows a typical result, where the measured spectrum is compared with the expected one. The latter spectrum was taken from the ISO calibration data base which includes a compilation of predicted spectra provided by M. Cohen or P. Hammersley (ISO website). For those objects not included in the data base we took one of the available models of a star of identical spectral type, and scaled the values to the K-magnitude of our object. In our sample of 43 normal star observations no excess due to hot circumstellar dust is expected (the sample also include the calibrator stars).

In Fig. 6 we show the measured-to-predicted ratios of 3 representative pixels for the whole sample. For each pixel the ratios above a brightness threshold (usually 5 Jy) were averaged and their standard deviation was computed. For the faint stars (below 1 Jy) the ratio values became too noise, and we computed the average and the standard deviation of the [Measured–Predicted] flux differences. The averages derived this way represent the

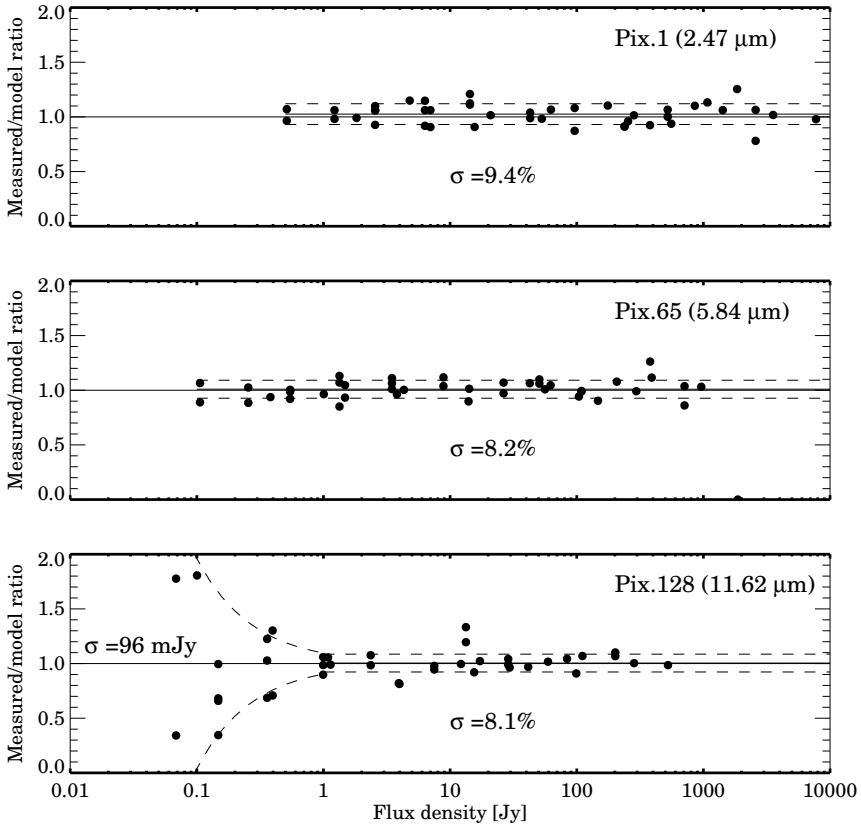

Fig. 6.— *Ratio of measured flux values to model prediction for 3 wavelengths (all normal star observations are included). Uncertainty values representative of the whole ensemble are computed separately at high flux level (expressed in %) and at low flux level (in mJy).*

typical systematic errors. We decided to correct for these systematic errors by dividing by the average flux ratio or by subtracting the average flux difference from all observations. This *empirical photometric correction* was the last step of the our post-processing sequence.

Error budget. The formal uncertainties provided by the automatic reduction in the ISO Archive do not contain several important sources of uncertainties, e.g. the ones related to the corrections in the post-processing. The average uncertainties in Fig. 7, on the other hand, do not represent the quality differences among observations (e.g. the effect of a particularly energetic cosmic glitch). As final photometric uncertainties, we decided to adopt the maximum of the two types of error bars. In practice, for most pixels/measurements the average uncertainty values are the higher.

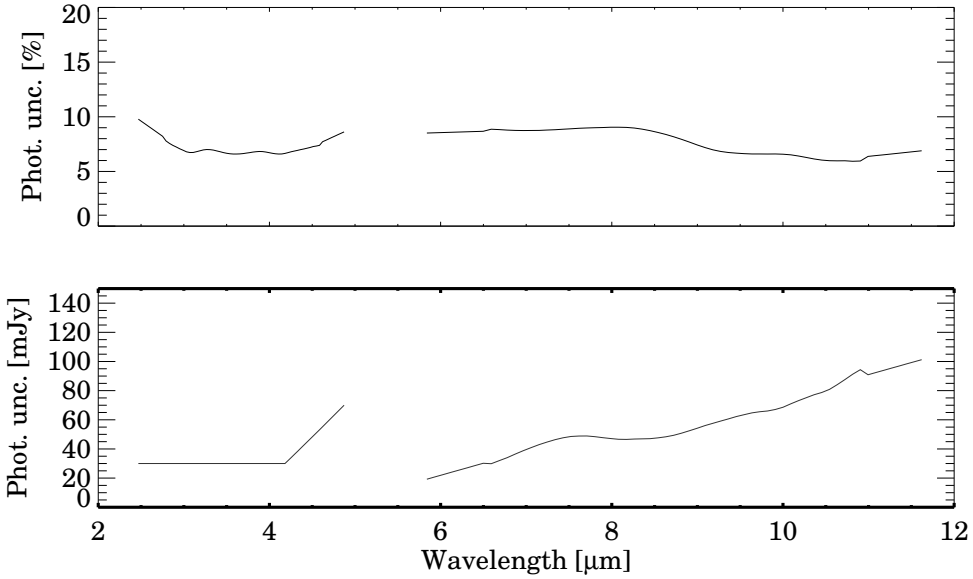

Fig. 7.— *Typical photometric uncertainties for the PHT-S wavelength range.*

During processing of certain observations we decided to cancel them from the main catalogue for various reasons (e.g. not recoverable memory effect, very large pointing offset, or no definite point source in the beam). Also, clear non-detections are not included in the catalogue. All the cancelled cases, with a short explanation of their problem, are listed in Appendix A.

REFERENCES

Acosta-Pulido J.A., Ábrahám P. 2003, in *The calibration legacy of the ISO Mission*, ESA SP-481, p. 95

Henning, Th.; Klein, R.; Launhardt, R.; Lemke, D.; Pfau, W., Astronomy and Astrophysics, v.332, p.1035-1043 (1998)

Mezger et al. 1992, A&A 265, p. 743-751

Murphy & Myers 2003, ApJ 591, 1034.

Visser, Richer & Chandler 2002, AJ 124, 2756

Appendix A

In Table 1 we present the main parameters of all the observations. The sources are divided into 4 groups according to their sub-class among young stellar objects.

The table contains of the following fields:

1. *Object name*: most popular name of the target in the literature.
2. *Coordinates (J2000)*: in order to obtain the most reliable coordinates for the infrared source, we checked the 2MASS all-sky release and picked up the closest bright source to the optical position.
3. *ISO_id*: the unique 8-digit identifier of an ISO observation in the ISO Data Archive. The asterisk following the ISO_{id} is a mark of some unusual observing parameter: either the detector temperature was outside the nominal range, or the observations was performed at the very beginning or the very end of the orbit. In both cases the photometric data are of reduced accuracy.
4. *Corrections*: in this column we summarize the type of corrections applied: M – memory correction; B – zodiacal background was predicted and subtracted; O – Off-centre position of the source in the beam. An exclamation mark signals cases when the correction might not be able to repair the full artifact due to a very serious effect.
5. *Observing date*
6. *SWS*: a pipe marks if ISO-SWS had also observed the source.
7. *Other name(s)* of the source used in the literature.
8. *Binary*: known binary systems are marked.
9. *Note*

Table 1. Young stellar objects observed with ISOPHOT-S

Object name	RA(2000) h m s	Dec(2000) ° ′ ″	Pos. ref.	ISO_id	Corr.	Obs. date	SWS	Other name	Note
Embedded YSOs of low and intermediate mass									
B5 IRS 1	03 47 41.60	+32 51 43.8	2MASS	63103703*	BO	08-Aug-97		NAME BARN 5 IRS 1	
L1489 IR	04 04 43.07	+26 18 56.4	2MASS	81401708*	O	07-Feb-98		NAME LDN 1489 IRS	
SVS76 Ser 4	18 29 57.73	+01 12 47.9	ISO	10803027*	MB	04-Mar-96		[SVS76] Ser 4	IR cluster
CK 1	18 29 57.74	+01 14 05.7	2MASS	10803126*	MBO	04-Mar-96		[SVS76] Ser 20	
CK 2	18 30 00.62	+01 15 20.1	2MASS	10803228*	M!BOE	04-Mar-96			
Low mass pre-main sequence stars									
T Tau	04 21 59.43	+19 32 06.4	2MASS	67901255	BO	25-Sep-97	√		
DG Tau	04 27 04.69	+26 06 16.3	2MASS	64501604*	B	22-Aug-97	√		
Haro 6-10	04 29 23.70	+24 33 02.0	2MASS	65300605	B	30-Aug-97			
				66901306	MBO	15-Sep-97			
HL Tau	04 31 38.43	+18 13 57.6	2MASS	65602507*	MB	2-Sep-97	√		
HD 34700	05 19 41.41	+05 38 42.8	2MASS	63602294*	B	13-Aug-97	√		
SX Cha	10 55 59.73	-77 24 39.9	2MASS	16600204	BO	1-May-96			
CR Cha	10 59 06.99	-77 01 40.4	2MASS	16600317	BO	1-May-96			
			2MASS	62501703	M!BO!	2-Aug-97			
CT Cha	11 04 09.09	-76 27 19.3	2MASS	16600124*	BO	1-May-96			
VW Cha	11 08 01.48	-77 42 28.8	2MASS	16700234*	BO	2-May-96			
Glass I	11 08 15.09	-77 33 53.1	2MASS	07900410*	MBO!	4-Feb-96			
				16600138*	BO!	1-May-96			
Ced 111 IRS 5	11 08 38.19	-77 43 51.7	2MASS	07900211*	BO!	4-Feb-96	√		
				62501412	M!BO	2-Aug-97			
VZ Cha	11 09 23.79	-76 23 20.7	2MASS	27101145	BO!	14-Aug-96			
CED 112 IRS 4A	11 09 53.40	-76 34 25.5	2MASS	62501217	MBO!	2-Aug-97		NAME CED 112 IRS 4	
WX Cha	11 09 58.73	-77 37 08.8	2MASS	16600749*	BO	1-May-96			
WW Cha	11 10 00.10	-76 34 57.8	2MASS	27101153	BO!	14-Aug-96			
XX Cha	11 11 39.65	-76 20 15.2	2MASS	16600664	BO	1-May-96			
CV Cha	11 12 27.72	-76 44 22.3	2MASS	58401637	BO	22-Jun-97			
				60601421	BO	14-Jul-97			
HD 98800	11 22 05.29	-24 46 39.8	2MASS	24001017	B	14-Jul-96	√		

Table 1—Continued

Object name	RA(2000) h m s	Dec(2000) ° ′ ″	Pos. ref.	ISO_id	Corr.	Obs. date	SWS	Other name	Note
WL 6	16 27 21.37	-24 29 48.3	2MASS	08101921*	BO				
S CrA	19 01 08.60	-36 57 20.0	2MASS	52301333	BO	22-Apr-97			
HH 100 IRS	19 01 50.67	-36 58 09.6	2MASS	11501029	BO	11-Mar-96	√	V710 CrA	
				70400629	BO	19-Oct-97			
VV CrA	19 03 06.74	-37 12 49.4	2MASS	52301015	BO	22-Apr-97			
Intermediate mass pre-main sequence stars									
VX Cas	00 31 30.68	+61 58 50.9	2MASS	58704023*	BO	25-Jun-97		HBC 329, SVS 3	uxor
IRAS 03260+3111	03 29 10.37	+31 21 59.1	2MASS	65201755	BO	5-Sep-97	√		
UX Ori	05 04 29.98	-03 47 14.2	2MASS	85801453	B	22-Mar-98			uxor
BF Ori	05 37 13.26	-06 35 00.5	2MASS	70101958*	B	17-Oct-97			uxor
RR Tau	05 39 30.51	+26 22 26.9	2MASS	67000863	BO	16-Sep-97			uxor
				86603163	BO	30-Mar-98			uxor
HD 95881	11 01 57.64	-71 30 48.4	2MASS	10400919	BO	29-Feb-96	√		
CU Cha	11 08 03.29	-77 39 17.4	2MASS	07900309*	MBO	4-Feb-96	√	HD 97048	
				14101580	BO	6-Apr-96			
				62501510	MBO	2-Aug-97			
HD 97300	11 09 50.03	-76 36 47.6	2MASS	07901912	MBO	4-Feb-96			
				62501316	MBO	2-Aug-97			
HD 100453	11 33 05.59	-54 19 28.5	2MASS	26000131*	B	2-Aug-96	√		
HD 100546	11 33 25.44	-70 11 41.2	2MASS	10400537*	BO	29-Feb-96	√		
HD 104237	12 00 05.10	-78 11 35.0	2MASS	10400325*	BO!	29-Feb-96	√	DX Cha	uxor
				23300625*	BO	7-Jul-96	√		
				53300118*	MB	2-May-97			
DK Cha	12 53 17.22	-77 07 10.6	2MASS	07901717	BO	4-Feb-96	√		
HD 135344	15 15 48.44	-37 09 16.0	2MASS	10401742	B	29-Feb-96	√		
				10401876	B	29-Feb-96			
HD 139614	15 40 46.38	-42 29 53.5	2MASS	10402322	BO	29-Feb-96	√		
HD 141569	15 49 57.75	-03 55 16.4	2MASS	62701662	B	4-Aug-97	√		
HD 142666	15 56 40.02	-22 01 40.0	2MASS	10402847	MBO	29-Feb-96	√		
HD 144432	16 06 57.96	-27 43 09.8	2MASS	10402662	BO	29-Feb-96	√		
HR 5999	16 08 34.27	-39 06 18.1	2MASS	28901748	MB	1-Sep-96	√		
WL 16	16 27 02.34	-24 37 27.2	2MASS	08100620	BO	06-Feb-96	√	BBRCG 19	

Table 1—Continued

Object name	RA(2000) h m s	Dec(2000) ° ′ ″	Pos. ref.	ISO_id	Corr.	Obs. date	SWS	Other name	Note
MWC 863	16 40 17.92	-23 53 45.2	2MASS	64102335*	B	18-Aug-97	√		
AK Sco	16 54 44.85	-36 53 18.5	2MASS	64402829*	BO	21-Aug-97	√		
MWC 865	16 59 06.77	-42 42 08.3	2MASS	28900460*	BO!	31-Aug-96	√	V921 Sco	
51 Oph	17 31 25.00	-23 57 46.0	2MASS	10301104*	MBO	28-Feb-96	√		
HD 163296	17 56 21.28	-21 57 21.8	2MASS	32901192	BO	10-Oct-96	√		
GGD 27	18 19 12.87	-20 47 30.5	ISO	14900325*	MB	14-Apr-96	√		IR cluster
HD 169142	18 24 29.78	-29 46 49.4	2MASS	13601437	MBO	1-Apr-96	√		
VV Ser	18 28 47.86	+00 08 34.6	2MASS	47800913	B	8-Mar-97			UXor
R CrA	19 01 53.15	-36 57 10.4	2MASS	11501230	O!	11-Mar-96	√	HBC 288	
T CrA	19 01 58.78	-36 57 49.8	2MASS	14100562	BO	6-Apr-96	√		
WW Vul	19 25 58.74	+21 12 31.3	2MASS	17600465	MBO!	11-May-96	√		UXor
			2MASS	51300108*	BO	12-Apr-97			
BD +40 4124	20 20 28.25	+41 21 51.4	2MASS	15900568	B	24-Apr-96	√		
LkHα 224	20 20 29.35	+41 21 26.6	2MASS	14201271	BO	7-Apr-96	√		
SV Cep	22 21 31.19	+73 40 27.0	2MASS	56201203	B	31-May-97	√		UXor
Eruptive young stellar objects (FUor, EXor)									
L1551 IRS 5	04 31 34.07	+18 08 04.9	2MASS	64201706*	MBO	19-Aug-97	√		FUor
UZ Tau	04 32 42.82	+25 52 31.4	2MASS	68401434	BO	30-Sep-97			EXor
				83300749	BO	25-Feb-98			
VY Tau	04 39 17.41	+22 47 53.3	2MASS	68101239	B	27-Sep-97			EXor
				83300854	B	25-Feb-98			
				86100859	B	25-Mar-98			
DR Tau	04 47 06.20	+16 58 42.3	2MASS	67901329	B	25-Sep-97			EXor
				83300944	B	25-Feb-98			

(*)Early/late orbital phase, reduced calibration accuracy

Appendix B

In this Appendix we discuss observations intially selected for our study but finally not included in the atlas. The descriptions below may give warnings to users of the ISO Data Archive concerning the quality and usefulness of these observations.

TMC 1 (ISO_id: 83501061). This 7-step scan, centred at α_{2000}=$4^h41^m42.49^s$, δ_{2000}=25°41′27.2″, crossed the TMC 1 molecular cloud. No excess emission from a compact source was, however, detected on the central position; all scan positions show similar background signals.

SM 1 FIR 3 (ISO_id: 49100625, 49100732). Figure 8 display two scans which cross each other at the position of a far-infrared source discovered by Mezger et al. (1992). Looking only at the North-South scan one could conclude on the existence of a source exhibiting PAH emission; but the East-West scan shows that the excess towards the centre of the map is related to another, somewhat extended strong source located at about 80″ to the West. No detection of SM 1 FIR 3 can be claimed.

Rho Oph B2 (ISO_id: 45801842). The 7-step scan exhibits no excess emission towards the central position α_{2000}=$16^h27^m27.6^s$, δ_{2000}=-24°26′56.0″ (Mezger et al. 1992) with respect to the neighbouring scan positions.

IRAS 16445-1352 (ISO_id: 81000624). Though the object name in the ISO Archive is "L158", the ISO position differs by 614″ from the SIMBAD coordinates of LDN 158, and coincides with the position of IRAS 16445-1352. This infrared source is classified in the literature either as a cirrus clump (e.g. Visser et al. 2002) or as a Class I source (Murphy & Myers 2003). After correcting for the zodiacal background the ISOPHOT-S spectrum shows no definite positive signal.

IRAS 17222-2404 (ISO_id: 83700725). Though the object name in the ISO Archive is "B74", the ISO position differs by 315″ from the SIMBAD coordinates of Barnard 74, and coincides with the position of IRAS 17222-2404. It is rather unknown source; there is no clear proof of its pre-main sequence nature. After correcting for the zodiacal background the ISOPHOT-S spectrum shows no definite positive signal.

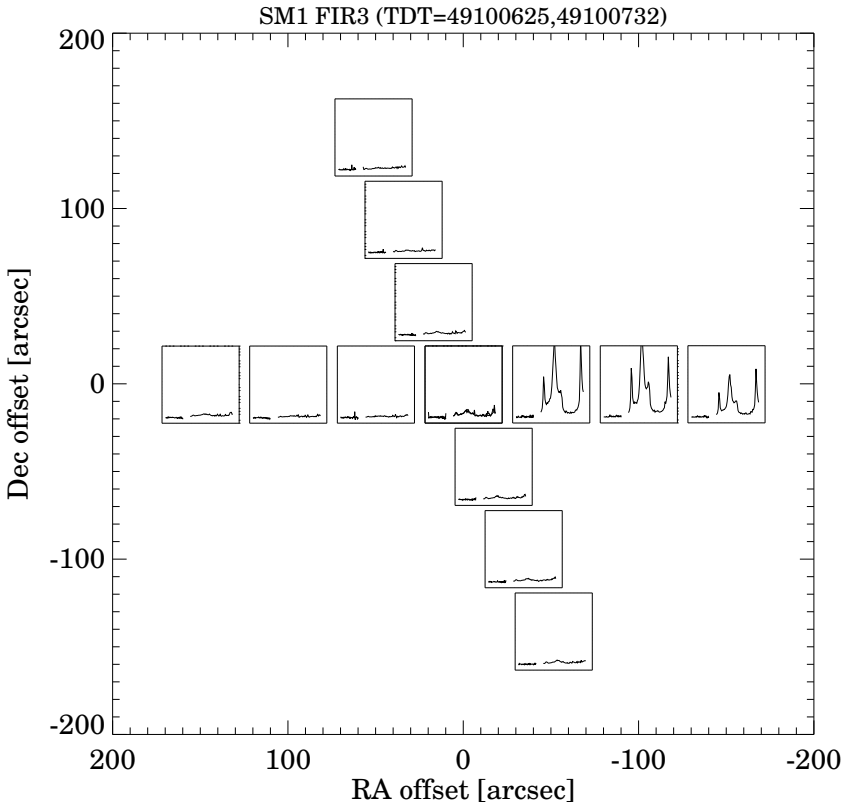

Fig. 8.— Typical photometric uncertainties for the PHT-S wavelength range.

M17 N (ISO_id: 49201553). The central position of this 7-step scan almost coincides with the position of M17 N IRS 2, an embedded source discovered at near-IR wavelengths by Henning et al. (1998). The ISOPHOT-S spectrum shows no definite positive signal towards the central raster step.